Supplemental Materials

Molecular Biology of the Cell

Rodriguez-Garcia et al.

Supplemental Figures

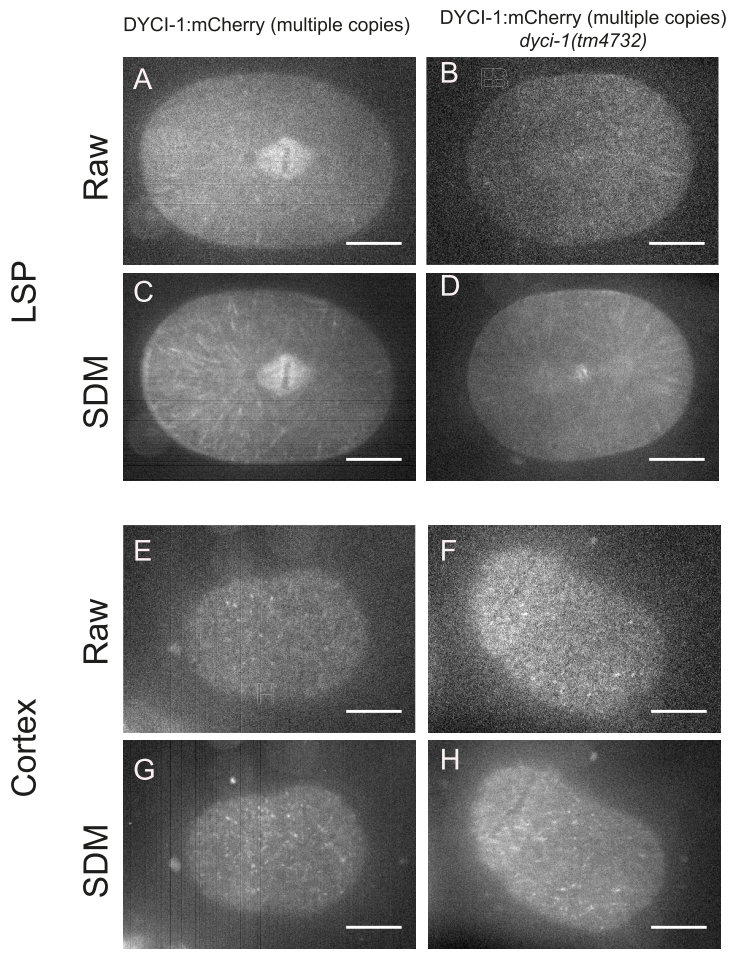

Figure S1: Micrographs of DYCI-1::mCherry in the lower spindle plane and at the cortex. Micrographs of randomly integrated DYCI-1::mCherry (**A,C,E,G**) in normal conditions and (**B,D,F,H**) after depletion of endogenous proteins through the homozygous *dyci-1(tm4732)* null mutation (Supplemental Text 1.2). The pictures in (A,B,E,F) are raw, while (C,D,G,H) are standard deviation maps (SDM, see Methods) obtained from 125 images acquired at 5 frames/s. Embryos were imaged in the lower spindle plane (LSP) (A-D) and at the cortex (E-H) by spinning disk microscopy. Scale bars, 10 μm.

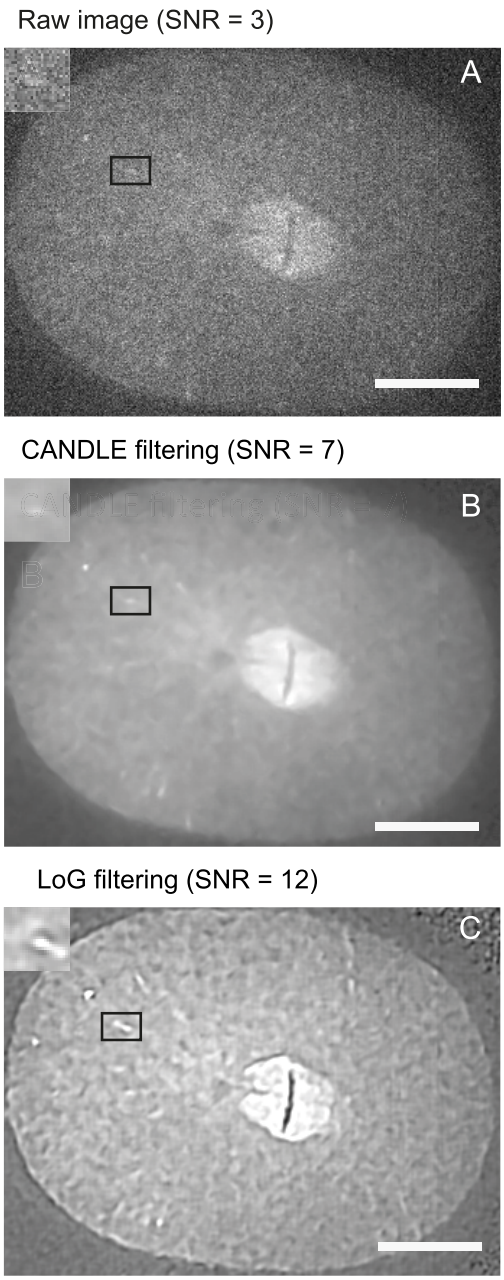

Figure S2: A typical DYCI-1::mCherry micrograph analyzed using our tracking pipeline. One-cell embryo during metaphase acquired after an exposure of 0.2 s, with signal-to-noise ratios (SNRs) indicated. Insets are magnified views of the regions delineated by black rectangles and each highlight a spot. Scale bars, 10 μm. The images were obtained at each step of pre-processing: (**A**) a raw picture; (**B**) an image denoised by the CANDLE filter; (**c**) an image after 2D LoG filtering (see Supplemental Text 2.1).

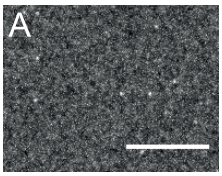

Simulated image
(SNR = 2)

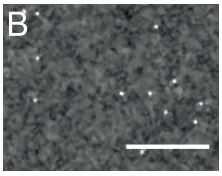

CANDLE filtering
(SNR = 7)

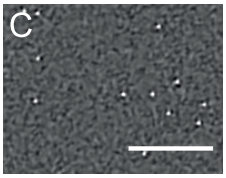

LoG filtering
(SNR = 8)

D

Tracking of simulated spots with directed motion

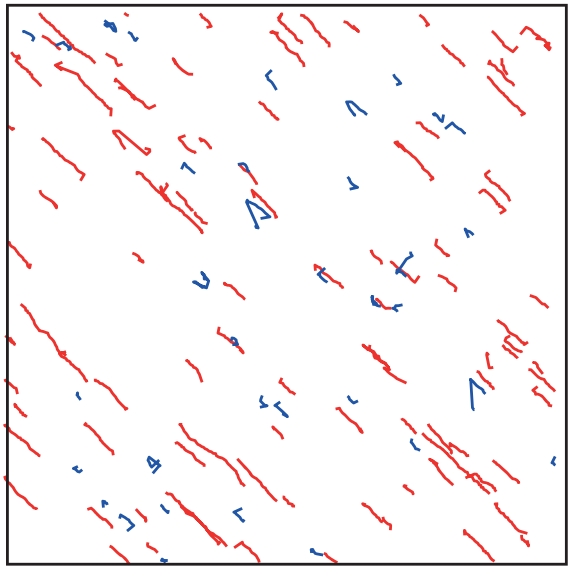

Tracks detected as directed
Tracks detected as diffusive-like

E

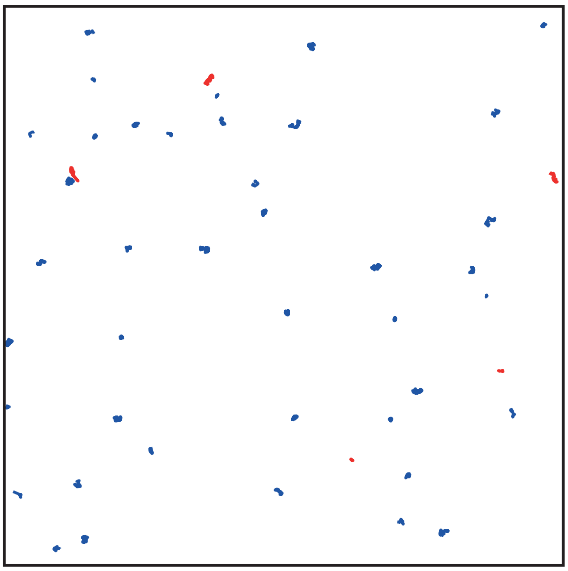

Tracking of simulated spots with diffusive motion

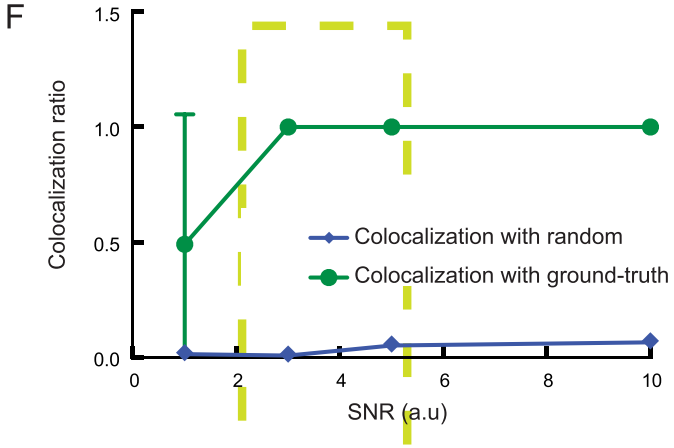

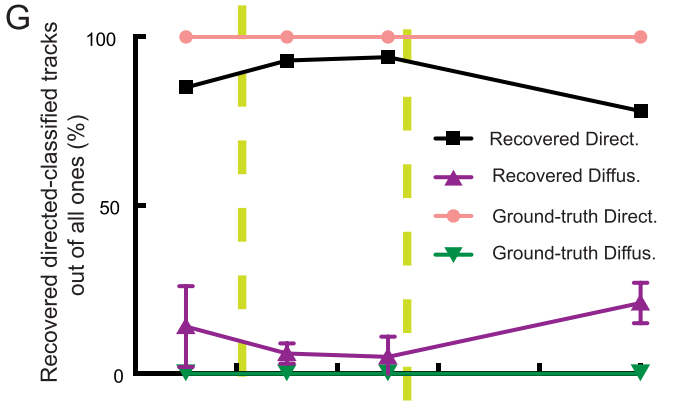

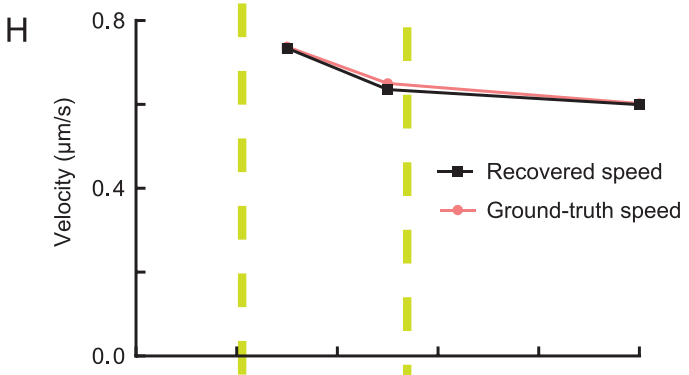

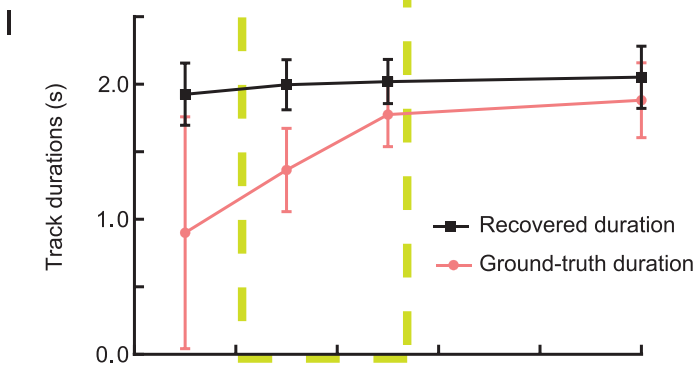

Figure S3: Validating our tracking pipeline through fabricated images that mimic experimental ones.

We used our pipeline using to analyze fabricated images with known spot dynamics and which mimic experimental ones (Supplemental Text 2). The signal-to-noise ratios (SNRs) are indicated, and the scale bars are 10 μm. The images were obtained at each step of pre-processing: (**A**) a raw picture; (**B**) an image denoised by the CANDLE filter; (**C**) an image after 2-D LoG filtering. (**D,E**) Typical tracking of two movies in which simulated spots displayed directed (D) and diffusive (E) motions. In both cases, the tracks recovered by our analysis pipeline are red for directed motion and blue for diffusive-like. **(F)** We first tested the colocalization of the tracks (green circles) compared to random colocalizations (blue diamonds). (**G**) We challenged the classification by computing the recovered percentages of the tracks classified as directed when analyzing simulated spots with directed (black squares) or diffusive-like (upward-pointing purple triangles) motion, compared to the set values in the simulation (pink circles and downward-pointing green triangles, respectively). From directed tracks, we compared the (**H**) average track speeds and (**I**) durations from both the simulation (ground-truth, pink circles) and from our analysis (black squares). The green-yellow dashed rectangle highlights the SNR values that correspond to our experimental observations. Error bars indicate the standard errors of the means.

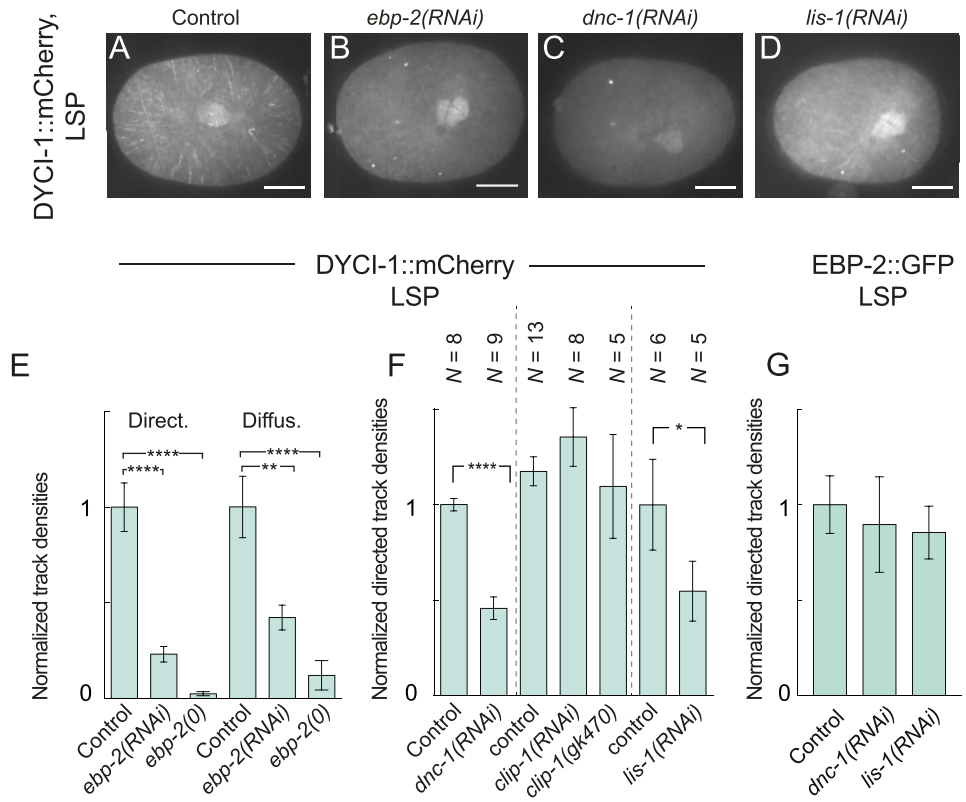

Figure S4: Dynein accumulates at the microtubule plus ends with the help of EBP-2^{EB}, dynactin, and LIS-1, but independently from CLIP-1^{CLIP170}.
(**A-D**) Maximum intensity projection computed from a 100-frame movie (5 frames/s) of **(A)** untreated DYCI-1::mCherry; **(B)** upon *ebp-2(RNAi)* treatment; (**C**) upon *dnc-1(RNAi)* treatment; and **(D)** upon *lis-1(RNAi)* treatment. Scale bars, 10 μm. (**E**) Trajectory densities for DYCI-1::mCherry in the lower spindle plane, divided between directed and diffusive-like motion (Supplementary Text 2.3), normalized by the mean in the corresponding control (Supplemental Text 2.4), upon partial *ebp-2(RNAi),* and after crossing with the *ebp-2(gk756)* null mutation. Data in the LSP are from $N = 8$ control; $N = 11$ *ebp-2(RNAi)*; and $N = 5$ *ebp-2(gk756)* embryos. (**F**) Similar experiment, analyzing directed tracks, in control, upon partial RNA interference of *dnc-1, clip-1,* and *lis-1,* and upon crossing with the *clip-1(gk470)* null mutant. (**G**) Similar analysis, analyzing directed tracks, imaging EBP-2::GFP and comparing $N = 8$ control embryos, $N = 6$ *dnc-1(RNAi)* dynactin subunits, and N = *10 lis-1(RNAi)*-treated embryos. Error bars indicate the standard errors of the means. Stars correspond to the statistical significances (see Methods).

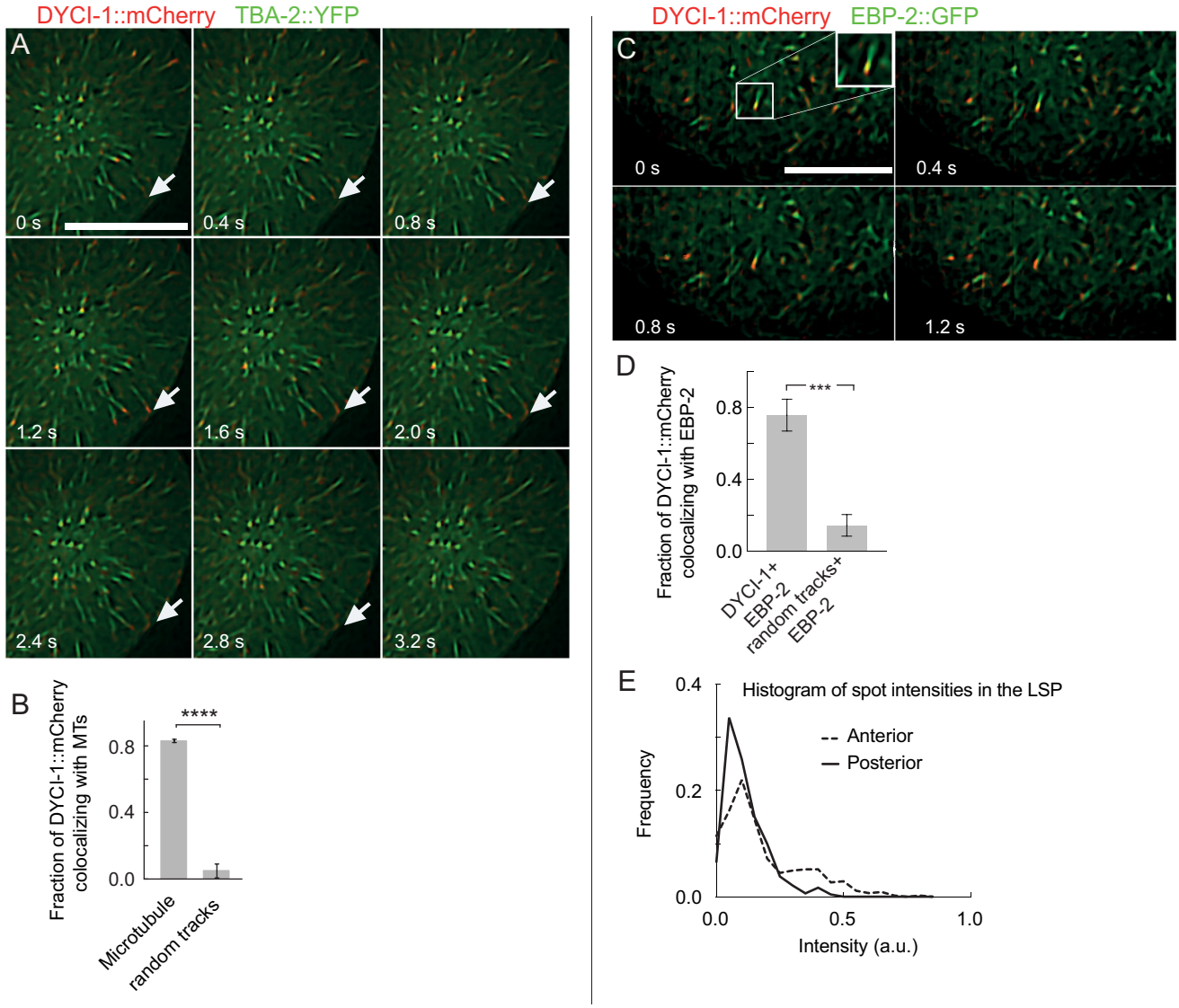

Figure S5: DYCI-1::mCherry colocalizes with microtubules and EBP-2::GFP at the microtubule plus ends.

(**A**) Sequence of micrographs acquired every 0.4 s displaying DYCI-1::mCherry (red) and TBA-2$^{\alpha\text{-tubulin}}$::YFP (green). Arrows indicate microtubule tips where DYCI-1::mCherry accumulates. Scale bar, 10 μm. (**B**) Fraction of DYCI-1::mCherry spots colocalizing with microtubules as compared to those colocalizing with simulated random tracks (Supplementary Text 3.2; N = 5 embryos, 9 stacks, 200 tracks). Statistical significance (p <10^{-4}) was computed with the Mann-Whitney/Wilcoxon test, and error bars show standard errors. (**C**) Sequence of micrographs of the metaphase of a *C. elegans* zygote, showing DYCI-1::mCherry (red) and EBP-2::GFP (green). Scale bar, 10 μm. (**d**) Percentage of DYCI-1::mCherry spots colocalizing with EBP-2::GFP (left, N = 9 embryos, 1880 tracks) compared to those colocalizing with simulated random trajectories. Statistical significance ($p \leq 0.001$)was calculated with the Mann-Whitney/Wilcoxon test. (**e**) Histogram of the intensities of the DYCI-1::mCherry spots in anterior and posterior embryo halves, measured in the LSP (N = 8 embryos).

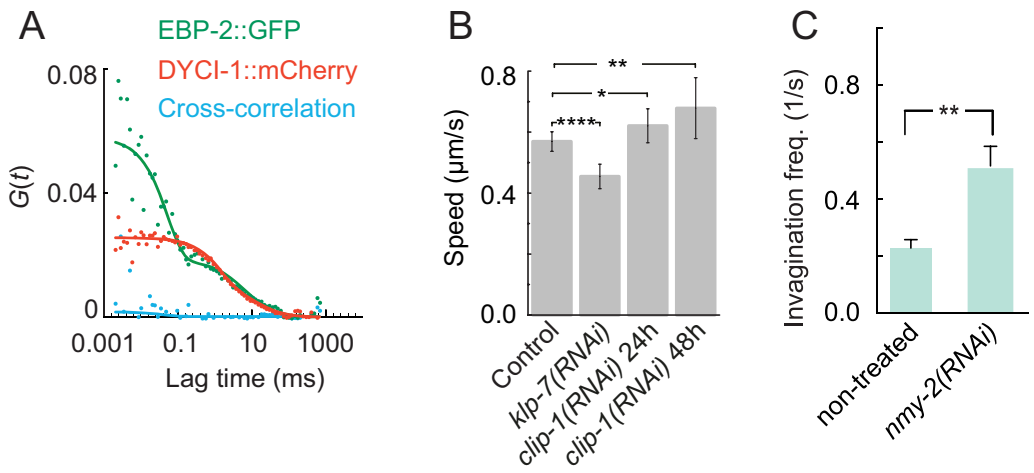

Figure S6: DYCI-1::mCherry and EBP-2::GFP are not attached in the cytoplasm; varying microtubule growth rates; validating the "tube assay."
(A) Autocorrelation of DYCI-1::mCherry (red dots) and EBP-2::GFP (green dots) measured by dual-color FCS. Experimental curves were fitted to a triplet-state model (Supplemental Equation S1) for each fluorescent species (plain lines, same colors). The cross-correlation curve and its fitting using the same model are blue. **(B)** Lower spindle plane velocity of DYCI::mCherry spots under four types of modulation of microtubule dynamics. Data typically come from 6 embryos and 1500 trajectories per condition. (**c**) Invagination frequencies in N =11 control embryos, and in N = 20 embryos in which the actin-myosin cortex was weakened by *nmy-2(RNAi)*.

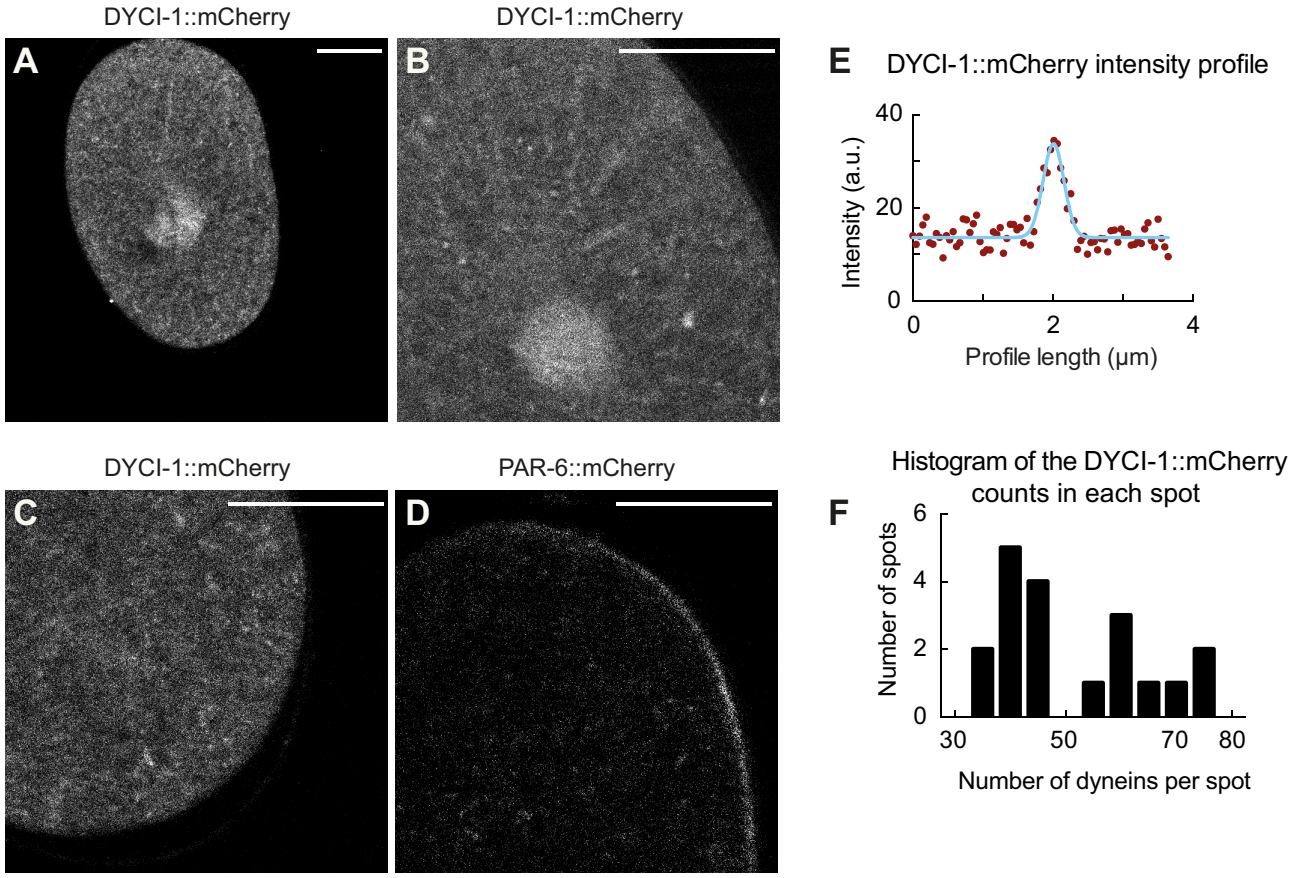

Figure S7: Using image intensity to count the number of dyneins per spot at the microtubule plus ends.
Typical micrographs of (**A-C**) randomly integrated DYCI-1::mCherry as those used to measure spot intensity profiles and (**D**) PAR-6::mCherry was used to calibrate intensity and convert it into a number of mCherry dyes. Scale bars, 10 µm. (**E**) Typical fit of a DYCI-1::mCherry spot intensity profile by a Gaussian distribution with background. (**F**) Histogram of the intensities of the DYCI-1::mCherry spots measured by the amplitude obtained through the fitted Gaussian distribution after the background was subtracted.

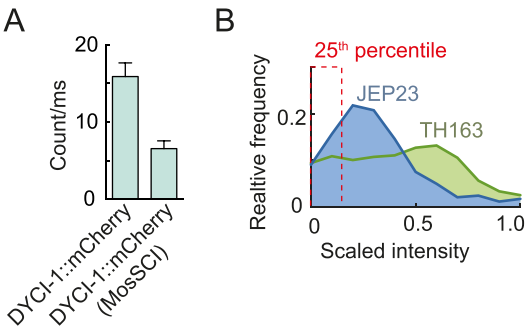

Figure S8: DYCI-1::mCherry expression levels and detection threshold.
(**A**) The average intensities (count/ms) in the cytoplasm obtained by FCS for TH163, the randomly integrated DYCI-1::mCherry (*N* = 6 embryos, 38 spots), and for JEP23, which carries exactly two copies of DYCI-1::mCherry (*N* = 10 embryos, 52 spots). Error bars represent the standard errors of the means. (**B**) Intensity histogram of the tracked spots in TH163 (green area, *N* = 6 embryos, 59 spots) and JEP23 (blue area, *N* = 6 embryos, 52 spots). The intensity values were scaled from 0 to 1 for plotting, with 0 the minimum value and 1 the maximum. The dashed red line represents the 25th percentile for JEP23, used as the detection threshold (Supplemental Text 2.6).

Movie Legends

Movie S1. One-cell embryo carrying a randomly integrated DYCI-1::mCherry imaged during metaphase at the LSP. The acquisition was done at 5 Hz by spinning disk microscopy, with no image processing. The movie was accelerated to 3x real-time. Scale bar, 10 μm.

Movie S2. One-cell embryo carrying a randomly integrated DYCI-1::mCherry imaged during anaphase at the LSP. The acquisition was done at 5 Hz by spinning disk microscopy, with no image processing. The movie was accelerated to 3x real-time. Scale bar, 10 μm.

Movie S3. One-cell embryo carrying a randomly integrated DYCI-1::mCherry imaged during metaphase at the cortex. The acquisition was done at 5 Hz by spinning disk microscopy, with no image processing. The movie was accelerated to 3x real-time. Scale bar, 10 μm.

Movie S4. One-cell embryo carrying a randomly integrated DYCI-1::mCherry and the homozygous *dyci-1(tm4732)* null mutation, imaged during metaphase at the LSP. The acquisition was done at 5 Hz by spinning disk microscopy, with no image processing. The movie was accelerated to 3x real-time. Scale bar, 10 μm.

Movie S5. One-cell embryo carrying a randomly integrated DYCI-1::mCherry and the homozygous *dyci-1(tm4732)* null mutation, imaged during metaphase at the cortex. The acquisition was done at 5 Hz by spinning disk microscopy, with no image processing. The movie was accelerated to 3x real-time. Scale bar, 10 μm.

Movie S6. Invaginations pulled from the cytoplasmic membrane towards the cell center in an embryo doubly labeled by DYCI-1::mCherry (left) and PLCδ1-PH::GFP (center) upon partial *nmy-2(RNAi)*. Right panel shows the superposition of the left and middle panels. The embryo was imaged at 2.5 Hz by spinning disk microscopy. Both channels were filtered by the CANDLE algorithm for better visibility. The movie was accelerated to 7x real-time. Scale bar, 10 μm.

Movie S7. Invagination at the cortex of an embryo acquired at 2.5 frame/s in a doubly labeled strain upon *nmy-2(RNAi)*. The green channel is PLCδ1-PH::GFP revealing the membrane, and the red is DYCI-1::mCherry. This movie is the source of the stills shown in Figure 3D.

Movie S8. Simulated fluorescence microscopy video depicting diffusive particles with exponentially distributed lifetimes, with a time constant of 10 s (Supplemental Text 2.4). The frame rate was 5 Hz, the signal-to-noise ratio was 5, and the movie was accelerated to 3x real-time. Scale bar, 10 μm.

Movie S9. Simulated fluorescence microscopy video depicting particles having direct motion and an exponential distribution lifetime, with a time constant of 10 s (Supplemental Text 2.4). The frame rate was 5 Hz the signal-to-noise ratio was 5, and the movie was accelerated to 3x real-time. Scale bar, 10 μm.

Movie S10. Embryo labeled with DYCI-1::mCherry (red) and EBP-2^{EB}::GFP (green), acquired at the LSP. The movie was filtered by the CANDLE and LoG filters (Supplemental Text 2.1), and accelerated to 7x real-time. Scale bar, 10 μm.

Movie S11. Embryo labeled with DYCI-1::mCherry (red) and TBA-2$^{\alpha\text{-tubulin}}$::YFP (green), acquired at the LSP. The inset is a zoom into the region delineated by the white square. The movie was filtered by

the CANDLE and LoG filters (Supplemental Text 2.1) and accelerated to 7x real-time. Scale bar, 10 μm.

Supplemental Text

to "The polarity-induced force imbalance in Caenorhabditis elegans embryos is caused by asymmetric binding rates of dynein to the cortex"

Ruddi Rodriguez-Garcia[a,b,*], Laurent Chesneau[a,*], Sylvain Pastezeur[a], Julien Roul[a,c], Marc Tramier[a], and Jacques Pécréaux[a,†]

[a]CNRS, Univ Rennes, IGDR (Institute of Genetics and Development of Rennes) – UMR 6290, F-35000 Rennes, France; [b]Present address: Cell Biology, Faculty of Science, Utrecht University, 3584 Utrecht, The Netherlands; [c]Present address: LAAS (Laboratoire d'analyse et d'architecture des systèmes), 31031 Toulouse, France.

*These authors contributed equally to this work.

†Address correspondence to J.P. (jacques.pecreaux@univ-rennes1.fr).

1. DYCI-1::MCHERRY IS A BONA FIDE REPORTER OF DYNEIN DYNAMICS

We set out to offer a detailed view of the dynamics of dynein at the microtubule plus ends and at the cortex, clarifying how it is targeted to the cell periphery, whether the involved mechanism is a transport mechanism, and understanding how dynein contributes to force imbalance at the cell cortex. To achieve this, we used a dynein light chain fluorescent reporter (Figure 1A-C, Supplemental Figure S1A,C,E,G and Movies S1-3), then did tracking and a detailed quantification (Figure 1F,G). To take full advantage of quantification, one must ensure that the fluorescent transgene faithfully reports all dynein localizations, without artefacts. It is equally important that the labeled and endogenous dyneins perform similarly, in particular in their contributions to the pulling forces generated at the cell cortex.

1.1. DYCI-1::MCHERRY IS A FUNCTIONAL TRANSGENE

To investigate the *in vivo* dynamics of dynein targeting to the cortex and its residence there, we used the TH163 strain carrying a randomly integrated transgene which encodes the fluorescently labeled DYCI-1::mCherry dynein sub-unit. This transgene was flanked by the endogenous regulatory sequences and produced within the framework of the TransgeneOme project (Sarov *et al.*, 2006; Sarov *et al.*, 2012). The fluorescence intensity in the one-cell embryo was variable, but there was no significant phenotype or lethality when compared to wild-type (N2, $N > 30$). Unlike in mammalian cells, DYCI-1 is the only intermediate dynein chain needed in the *C. elegans* zygote, and its PANTHER-identified paralog C27F2.1 (Mi *et al.*, 2010; Mi *et al.*, 2013) has no early embryo phenotype (Kamath *et al.*, 2003; Sonnichsen *et al.*, 2005). We can therefore expect this transgene to report dynein in all its functions.

1.2. THE DYCI-1::MCHERRY TRANSGENE RESCUES THE RECESSIVE EMBRYONIC LETHAL NULL MUTATION *DYCI-1(TM4732).*

We first aimed to validate the functioning of the randomly integrated transgene by using it to rescue the *dyci-1(tm4732)* recessive lethal null mutation. We began by producing JEP9 by crossing the heterozygous strain carrying the *dyci-1(tm4732)* null mutation with the VC2542 strain. This latter carries a balancer featuring a pharynx/gutGFP marker and the re-arrangement nT1[qIs51] which prevents the homozygous hermaphrodite from reproducing (and two wild-type *dyci-1* copies). The JEP9 strain showed a lethality rate of 48.8±7.9% (N = 3 replicas, 302 hermaphrodites), which suggested that homozygous *dyci-1(tm4732)* should be 100% lethal. This was confirmed by counting the GFP-negative larvae in JEP9 progeny, i.e. those homozygous for *dyci-1(tm4732)*. We found a frequency of 0.3±0.3% (N = 3 replicas, 498 hermaphrodites).

We then obtained JEP40 by crossing JEP9 twice with TH163, a randomly integrated DYCI-1::mCherry strain. JEP40 has only mCherry-labeled *dyci-1* genes, without the endogenous copy. This displayed a reduced embryonic lethality, 20.5 ± 7% (N = 3 replicas, 123 hermaphrodites), and some dpy/unc phenotypes. In this strain, we noticed a variation in fluorescence intensity, so we decided to explore expression levels. With the help of the Biology of *Caenorhabditis elegans* facility (UMS3421, Lyon, France), we used MosSCI to design JEP23, a strain carrying exactly two copies of the above transgene (Boulin and Bessereau, 2007; Robert and Bessereau, 2007). For this purpose, the DYCI-1::mCherry sequence (consisting of 3035 nucleotides from before the dyci-1 5'UTR to the end of the 3'UTR) was amplified from TH163 genomic DNA, cloned into the AflII/BglII site of the pCFJ352 plasmid, and bombarded into the EG6701 strain. Integration on the ttTi4348 MosSCI site was verified by sequencing. We twice crossed this JEP23 strain with the *dyci-1(tm4732)* null mutation JEP9 to produce JEP30. Worms homozygous for dyci-1::mCherry insertion and heterozygous for the *dyci-1(tm4732)* null mutation produced viable null mutant homozygote worms, whose progeny displayed 81.1±14.2% lethality (N = 3 replicas, 21 hermaphrodites). We concluded that the DYCI-1::mCherry transgene products could perform all of the roles of DYCI-1.

We then focused on the phenotypes of the progeny of the two homozygous *dyci-1(tm4732)* strains at the one-cell stage. The first one, JEP40 also carrying randomly integrated DYCI-1::mCherry, had no particular phenotype (Supplemental Figure S1B,D,F,H, and Movies S4-5). In contrast, the second strain, JEP30, has exactly two copies of dyci-1::mCherry, and in the second generation it displayed a phenotype at the one-cell stage reminiscent of a partial DYCI-1 depletion. Indeed, it this phenotype is similar to that of *dyci-1(RNAi)* when observed between 12 and 19 h after transfer onto feeding plates. Going further, we quantified JEP30 phenotype and rarely observed more than 2 pronuclei (2/11 embryos). In embryos with two pronuclei, the meeting happened in 6/9 embryos. In these, the spindle was often ill-formed (5/6) but still migrated at least partially to the cell center and oriented along the anteroposterior axis (4/6) prior to the onset of cytokinesis. Initial furrow ingression was well-positioned (4/6). Overall, we concluded that the one-cell stage *dyci-1(tm4732)* phenotype is rescued by the dyci-1::mCherry construct, although when present in exactly two copies, the expression level of the DYCI-1::mCherry transgene might be too low.

1.3. MEASURING CYTOPLASMIC DYNEIN CONCENTRATIONS

As part of our attempt to decipher the dynein targeting mechanism and how it contributes to supplying these molecular motors to the cortical pool and to pulling force generation, we estimated the cytoplasmic dynein concentrations for each embryo half. Fluorescence correlation spectroscopy (FCS) traces (Figure 2C) were analyzed using SymPhoTime (PicoQuant). We fitted the autocorrelation function $G(\tau)$ using a triplet-state model for one fluorescent species (Widengren *et al.*, 1994) as follows:

$$G(\tau) = G(0)\left[1 - T + Te^{\left(-\frac{t}{\tau_T}\right)}\right]\left(1 + \frac{t}{\tau}\right)^{-1}\left(1 + \frac{t}{\tau\kappa^2}\right)^{-1/2} \quad \text{(S1)}$$

where t is the lag time; T is the triplet decay fraction; τ_T is the lifetime of the triplet state; τ is the diffusion time of the fluorescent species; κ is the length-to-diameter ratio of the focal volume set to 4. We calculated the cytoplasmic concentration as $C = \frac{1/G(0)}{V_{eff}N_A}$, where V_{eff} is the effective excitation volume and N_A is the Avogadro constant. Using the strain doubly labeled with DYCI-1::mCherry and EBP-2::GFP, we found 32 ± 11 particles in the focal volume (N = 8 embryos, 38 spots), estimated at 0.3 fl, yielding a concentration of approximately 177 ± 60 nM.

1.4. USING TWO INDEPENDENT APPROACHES FOR COUNTING MOLECULES BOUND TO THE MICROTUBULE PLUS-ENDS

We next investigated how many dyneins molecules are present in a single spot at a microtubule plus end in the LSP. To do so, we used FCS. Because of the weak fluorescence intensity of the DYCI-1::mCherry spots, it can be challenging to detect peaks that correspond to a dynein spot crossing the FCS volume. We therefore used strain doubly labeled with DYCI-1::mCherry and EBP-2::GFP, and EBP-2 revealed the spot positions. The parameters obtained for association kinetics (see 4.1, Figure 2D) were plugged into equation S1 above, along with the previously measured cytoplasmic concentrations (see 1.3). This resulted in an estimate of 66 ± 5 particles per spot. In comparison, in the same experiment we measured 82 ± 38 EBP-2::GFP molecules in the 0.3 fl FCS volume, corresponding to 185 ± 85 EBP-2::GFP per spot (N = 8 embryos, 38 spots). This is consistent with the previously calculated count for DYCI-1::mCherry, which is assumed to be indirectly bound to EBP-2. In the strain carrying exactly two DYCI-1::mCherry copies on top of endogenous DYCI-1, there were 29 ± 6 dyneins per spot (N = 5 embryos, 66 spots).

To strengthen our results, we tried a different approach, this time based on comparing spot intensities to a reference (Shivaraju *et al.*, 2012). We used the PAR-6::mCherry strain as a reference and calibrated intensity in order to convert the result into a particle count. We did this by comparing

the background intensities in the images of this strain (Supplemental Figure S7D) with the cytoplasmic concentrations measured by FCS as described above (N = 8 embryos, 16 spots). We then imaged the strain carrying randomly integrated DYCI-1::mCherry (TH163) in identical conditions (Supplemental Figure S7A-C), fitting the dynein spot intensity profiles by a Gaussian distribution with an additional constant b representing the background:

$$I = (A-b)\mathrm{e}^{\frac{(x-\bar{x})^2}{2\sigma^2}} + b \qquad \text{(S2)}$$

where x is the spot's position in the intensity profile, σ is its width (Supplemental Figure S7E), and A the amplitude of the peak. We repeated this experiment, and plotted the corresponding histogram of background-subtracted amplitudes (A-b) (Supplemental Figure S7F). The resulting average was 50 ± 13 DYCI-1::mCherry particles per spot (N = 6 embryos, 20 spots) in TH163. Assuming that the doubly labeled strain displays similar dynein counts in the spots as TH163, this estimate is consistent with the one obtained above.

Overall, our data show that the randomly integrated DYCI-1::mCherry transgene, herein referred to simply as DYCI-1::mCherry, is a *bona fide* dynein reporter, instrumental for investigating dynein's dynamics both in the cytoplasm and at the cortex.

2. IMAGE PROCESSING PIPELINE FOR MEASURING DYNEIN DYNAMICS

2.1. PRE-PROCESSING THE IMAGES

Since dynein spots are very weak, we denoised the images to filter out the contributions from the cytoplasmic fraction and to increase the signal-to-noise ratio. Noise reduction in this manner usually relies on the assumptions that the noise is non-correlated in space and time and that it follows a Gaussian or Poisson distribution. Because there is a minimum number of dyneins per spot before one can detect them, the spots under this threshold might contribute to the background. Furthermore, because these objects are large in comparison to the dynein in the cytoplasm, they can create a correlated background "noise" in space and time. We therefore opted to use CANDLE filtering/denoising (Coupe *et al.*, 2012) (Supplemental Figure S2a,b) to avoid the noise issues. We used the following parameters, which allowed for a proper view of the fine structures and enabled the distinction of close individual spots: a smoothing parameter beta of 0.05; a patch radius of 1 (3x3x3 voxel); and a search volume radius of 3. We used the fast processing of the dark background since normal processing did not improve the images. The processed images were then submitted to spot enhancement (Sage *et al.*, 2005) using a Laplacian of Gaussian filter with standard deviation σ = 1.25 (Supplemental Figure S2C).

2.2. AUTOMATED TRACKING OF DYCI-1::MCHERRY FLUORESCENT SPOTS.

Because multiple tracks are present and could cross each other, we needed an algorithm with robust linking. We opted for u-track (Jaqaman *et al.*, 2008) using the parameters shown below (Supplemental Table S1). We validated these parameters by analyzing fabricated images having known dynamics (see 2.5). When observing the LSP, we excluded the spindle, which we obtained from a semi-supervised segmentation. Because we were conservative in the u-track algorithm parameters, it is possible that some long tracks were broken into pieces.

Detection	
Gaussian standard deviation	Iterate to estimate Gaussian standard deviation. Maximum number of iterations 10
Rolling window time-averaging	3
Iterative Gaussian mixture-model fitting	No

Tracking	
Maximum gap to close	LSP (8), cortex (3)
Merge split	0
Minimum length of track segments from first step	LSP (3), cortex (6)
Cost function for frame-to-frame linking	
Flag for linear motion	1
Allow instantaneous direction reversal	LSP (0), cortex (1)
Search radius lower limit	2
Search radius upper limit	5
Standard deviation multiplication factor	1
Nearest neighbor distance calculation	1
Number of frames for nearest-neighbor distance calculation	9
Cost function to close gaps	
Flag for linear motion	1
Search radius lower limit	2
Search radius upper limit	5
Standard deviation multiplication factor	3
Nearest-neighbor distance calculation	
Number of frames for nearest-neighbor distance calculation	9
Penalty for increasing gap length	1.5
Maximum angle between linear track segments	30

Supplemental Table S1: The u-track software parameters used in this study.

2.3. TRACK CLASSIFICATION

To characterize the dynamics of the spots, we classified the tracks according to two features: (1) the directionality; (2) the moving sense (centrifugal/centripetal).

Classification of tracks according to their asymmetry.

Visual inspection of tracks (Figures 1F, 5E) suggested that some might be directed. We therefore divided them between anisotropic (directed) or isotropic (diffusive-like), based on their asymmetrical trajectories and as per the method proposed in (Huet *et al.*, 2006). Tracks shorter than 3 frames (at the cortex) or 5 frames (in the LSP) were ignored. We chose an alpha parameter (the classification threshold) of 0.1 (90^{th} percentile).

Classification of linear trajectories according to their moving sense.

We expected different molecular mechanisms in the directed motion of tracks causing motion in different ways, either towards the center or the periphery. To classify these trajectories according to their motion sense, we first segmented the embryo contour using a supervised segmentation. For each track, we computed the Euclidean distance between each track point and the embryo contour curve, which forms a vector listing the distances to the cortex that is of the same length

as the track itself. The differences between adjacent elements in the vector were used to reveal whether a step in the track brought the spot closer to or farther from the cortex. We then computed the probability θ of moving towards the cortex as the ratio between the number of steps that contributed to getting the spot closer to the cortex and the total number of steps in the track. Tracks with results above 0.7 were declared to be moving towards the cell cortex. Similar ratios and thresholds were used, *mutatis mutandis*, to classify tracks moving towards the centrosome. When doing so, we discarded the few tracks that showed no clear direction. Figure 1G shows a good example of the results.

2.4. NORMALIZED DENSITY AND FREQUENCY OF THE TRACKS

To compare dynein tracks in various conditions, we computed either the density or the frequency of the tracks at the cortex:

The **Frequency** represents the number of tracks measured at the cortex, or in a cortical region, divided by the duration of the movie. When focusing on the diffusive population (see the two last sections of the Results in the main text), this quantity directly shows the average number of dyneins engaging in force generation per second, independently of their residence time. This is the relevant quantity when investigating the imbalance in the number of active force generators.

The **Density** corresponds to the above frequency divided by the area of the region (or of the whole imaged cortex), in which the tracks were counted. This quantity is adequate for determining whether a treatment decreases the number of dyneins tracks at the cortex to ensure independence from embryo size changes, which, although moderate, can occur upon RNAi or mutation and would bias the analysis.

Finally, because the level of expression of DYCI-1::mCherry was variable (see 1.1), each treatment was paired with a control, and this one was used to **normalize** the results: all densities and frequencies were divided by the density or frequency of the control, respectively. When comparing multiple regions (Fig. 5 and in the last section of the Results), we used the anterior-most region as the reference.

2.5. ANALYZING SIMULATED MICROSCOPY IMAGES TO VALIDATE THE ANALYSIS PIPELINE.

To ensure that our image processing pipeline faithfully describes spot dynamics, we created synthetic fluorescent images which mimicked our experimental data (Costantino *et al.*, 2005) (Supplemental Figure S3A). We simulated the stochastic trajectories of particles, which either underwent a pure diffusion as per $x_{i,j}(t+1) = x_{i,j}(t) + \xi\sqrt{2Dt}$ (Movie S8), or a diffusion with an added flow, $x_{i,j}(t) = x_{i,j}(t) + \xi\sqrt{2Dt} + v_{i,j}t$ (Movie S9). Here, $x_{i,j}(t)$ represents the coordinates in two dimensions at time *t*; where ξ is a random number; *D* is the diffusion coefficient; and $v_{i,j}$ is the flow speed. The track durations (lengths) were sampled from an exponential distribution. The intensity was set to be similar to the experimental one and was encoded by the Qyield quantum yield parameter. We plotted the instantaneous positions and applied a Gaussian filter to mimic the effect of the point-spread function in fluorescence microscopy. We then added two types of noise. First, we imitated the background noise by adding to each pixel a sampling of a Gaussian distribution normalized to ε, as per the formula $A_{noisy} = A + \epsilon M$ and corresponding to a signal-to-noise ratio of $\max(A)/\varepsilon$. Secondly, we mimicked the fluorescence background by superimposing a large number of fast-diffusing particles on the noisy image. This simulation provided a realistic scenario for testing the image processing and data analysis pipeline, and details of the parameters used are listed in Supplemental Table S2.

Image size	250 x 250 pixels

Duration	100 frames (20 s)
Density of particles (tracks)	(0.15 particles/μm^2)
Density of fast-diffusing background particles	900 particles/μm^2
Qyield	0.42 (mCherry)
Pixel size	0.130 nm
Sampling rate	0.2 s
PSF type	Gaussian
PSF size	0.3 μm
Bits	12
Diffusion coefficient	0.002 μm^2/s
Flow speed (*x* and y coordinate)	0.4 μm/s
Background noise standard deviation, σ	0.1; 0.3; 0.5; 0.7
Mean track lifetime (mean of exponential distribution)	10
Diffusion coefficient of the background particles	2.1 μm^2/s
Mean track lifetime (mean of exponential distribution) for background particles	2 s

Supplemental Table S2: Parameters for the images of simulated dynein dynamics.

We pre-processed the fabricated images as we had the real ones (Supplemental Figure S3B,C), then analyzed them (Supplemental Figure S3D,E). A comparison of the two datasets recovered by our analysis pipeline and from the simulation (ground-truth results) suggests that the analysis pipeline performed well in the signal-to-noise ratio range corresponding to the experimental images (Supplemental Figure S3F-I).

2.6. ESTIMATING THE DETECTION THRESHOLD

We figured that the large cytoplasmic concentration of dynein might limit our ability to detect spots made of a low number of DYCI-1::mCherry. To delineate our detection limit, we computed the detection threshold by first considering the microtubule plus-end spot intensities in JEP23, the strain having exactly two copies of DYCI-1::mCherry integrated by MosSCI. We assumed that the spot intensities were distributed normally above a constant background. We fitted the histogram of spot intensities using a Gaussian distribution with an added constant, for both JEP23 (N = 6 embryos, 41 spots) and the TH163 randomly integrated DYCI-1::mCherry-carrying strain (N = 6 embryos, 52 spots). The added constant values corresponded to the background levels. We next subtracted the respective background levels from the spot intensity distributions for each strain and computed the 25th-percentile (Supplemental Figure S8B). To be conservative, we used the result as the intensity-detection threshold. To convert this value into a particle count, we assumed that after subtracting the background, the average of the intensity distribution of the doubly labeled DYCI-1::mCherry; EBP-2::GFP strain is the same as that of JEP23. In other words, the $P_{MT\text{-}tip}$ results for DYCI-1::mCherry (see 4.1) were assumed to be equal for both strains. We could thus associate a number of particles to the average DYCI-1::mCherry spot intensity in JEP23 using the estimate for the doubly labeled strain (see 1.4), and therefore to JEP23's 25th percentile intensity distribution. In this case, the result was a threshold of 26 ± 4 particles.

3. DYNEIN IN THE CYTOPLASM

3.1. DYNEIN ACCUMULATES AT THE MICROTUBULE PLUS ENDS WITH THE HELP OF EBP-2, DYNACTIN, AND LIS-1, BUT INDEPENDENTLY OF EBP-1/-3 AND CLIP-1^{CLIP170}.

Because DYCI-1::mCherry displayed similar dynamics to EBP-2::GFP and colocalized with it (main text, Supplemental Figure S5C,D), we set out to confirm that that dynein uses EBP-2^{EB} to track microtubule plus ends, as previously reported (Barbosa *et al.*, 2017; Schmidt *et al.*, 2017). Furthermore, *in vitro* experiments using purified human proteins (Duellberg *et al.*, 2014) suggest that in higher eukaryotes dynein tracks the microtubule plus ends via a hierarchical interaction involving binding to dynactin, which in turn binds to EB1 with the help of CLIP170. We investigated the mechanism in *C. elegans* by crossing the DYCI-1::mCherry strain with one carrying the *ebp-2(gk756)* null mutation. In this way, we obtained a viable strain without dynein spots in the cytoplasm, although some faint spots below our detection limits may remain (Supplemental Figure S4D). We also depleted EBP-2 by RNAi and obtained similar results (Supplemental Figure S4A,B,E). To further test whether dynein hitches a ride with EBP-2, either directly or with the help of accessory proteins, we depleted dynactin and LIS-1 by *dnc-1$^{p150/glued}$(RNAi)* and *lis-1(RNAi)*, respectively. These RNAi were partial, to preserve the early steps of mitosis. We observed a strong reduction in the LSP-directed track densities (Supplemental Figure S4A,C,D,F), and as expected the treatment resulted in a strong phenotype reminiscent of dynein depletion (Skop and White, 1998; Cockell *et al.*, 2004). In contrast, EBP-2::GFP plus-end accumulation was not affected by these same treatments (Supplemental Figure S4G), which is consistent with the previous observation that microtubule growth rates remain unaltered (Srayko *et al.*, 2005). Because these results are similar to those proposed in higher eukaryotes, we wondered about the role of CLIP-1^{CLIP170}. Surprisingly, neither treatment with *clip-1(RNAi)* nor crossing with a strain carrying the *clip-1(gk470)* null mutation resulted in any significant alteration of the track densities (Supplemental Figure S4F). We concluded that dynein accumulates at the microtubule plus ends via EBP-2^{EB} with the help of dynactin and LIS-1, which resembles the findings in mammal protein experiments (Duellberg *et al.*, 2014). Using human proteins, CLIP170 was identified as promoting the hierarchical interaction *in vitro,* but it may not have a role in nematodes, consistent with the previously reported result (Barbosa *et al.*, 2017).

3.2. COLOCALIZATION

We crossed the strain carrying randomly integrated DYCI-1::mCherry with ones carrying either TBA-2::YFP or EBP-2::GFP. We found that most of the DYCI-1::mCherry spots colocalized with microtubule plus ends and EBP-2::GFP in the doubly labeled strains (Supplemental Figure S5A-D and Movie S10-11). We tracked spots on both channels, setting as colocalized those spots that are closer than 4 pixels at each time. We studied only those tracks longer than 6 time-points and which displayed directed motion, although we reduced the threshold track length to 3 points for cortical colocalizations. In all cases, we wondered whether the high density of DYCI-1::mCherry spots might cause artefactual colocalization. Therefore, for each colocalization experiment, we compared the results with the colocalization of a synthetic set of spots of identical count (Jaqaman *et al.*, 2011). In the present case, we found a very significant difference (Supplemental Figure S5B,C), indicating that colocalization cannot be explained by incidental encounters. Furthermore, by using dual-color fluorescence correlation spectroscopy on the EBP-2::GFP; DYCI-1::mCherry doubly labeled strain, we observed peaks of fluorescence in some intensity tracks. The peaks represent the microtubule plus ends crossing the focal volume. We found that these two proteins crossed the focal volume simultaneously (Figure 2C). This suggests that dynein and EBP-2 share a common position at the growing microtubule plus ends.

4. DYNEIN DYNAMICS AT THE PLUS ENDS

4.1. MEASURING DYNEIN BINDING RATES AT MICROTUBULE PLUS ENDS.

To analyze the dynamics of dynein spots and estimate the binding rate of dynein to a microtubule plus end, we followed (Dragestein, 2008), fitting the number of units bound at the plus end versus the concentration in the cytosol nearby with the equation:

$$P_{MT-tip} = Y_{max}\left(1-\mathrm{e}^{-kP_{cytosol}}\right) \qquad \text{(S3)}$$

where $P_{MT\text{-}tip}$ is the number of units (DYCI-1::mcherry) at the plus end of the microtubule; $P_{cytosol}$ is the cytoplasmic concentration within the FCS focal volume; k is the binding rate; and Y_{max} is the maximum number of units at the plus end. We measured the cytoplasmic concentration as detailed above (see section 1.3). The number of particles in the peak was obtained proportionally, by using the ratio of peak-to-basal intensity in the FCS trace (e.g. Figure 2C). In doing so, we assumed that the basal intensity corresponds to the cytoplasmic concentration. We analyzed 43 spots in 8 embryos of the double-labeled DYCI-1::mcherry; EBP-2::GFP strain and fitted the respective measurements with equation S3 for each channel. DYCI-1::mcherry and EBP-2::GFP displayed similar dynamics, particularly their binding rates which were $k^{DYCI\text{-}1} = 0.006$ and $k^{EBP\text{-}2} = 0.003$ (Figure 2D).

4.2. CHARACTERIZING DYNEIN UNBINDING DYNAMICS AT THE MICROTUBULE PLUS ENDS BY MODULATING MICROTUBULE GROWTH RATES.

We set out to measure the detachment of dynein from microtubule plus-ends, and how this compares to the known EBP-2^{EB} dynamics (Bieling *et al.*, 2007; Akhmanova and Steinmetz, 2015). In other words, how does the length of the "comet tail" of plus-end dynein accumulation vary when microtubule growth rates change? We plotted an intensity profile across dynein spots and used an exponential fit to measure the characteristic length of the comet tail. To change microtubule growth rates, we used hypomorphic RNAi of *klp-7*^{mcak} and *clip-1*^{clip170}, which are genes that alter microtubule dynamics (Supplemental Figure S6B) (Srayko *et al.*, 2005). Importantly, upon penetrant RNAi, we did not see dynein depletion from the plus ends. In particular, we measured "comet tail" lengths under four conditions (ordered by decreasing microtubule growth rates): *clip-1(RNAi)* during 48 h (N = 5 embryos, 3960 spots, 58 profiles); *clip-1(RNAi)* during 24 h (N = 6 embryos, 2781 spots, 30 profiles); untreated embryos (N = 8 embryos, 3000 spots, 30 profiles); and *klp-7(RNAi)* during 24 h (N = 6 embryos, 1067 spots, 30 profiles). Through this experiment (see main text), we suggest that dynein displays a dynamics similar to EBP-2^{EB} one at microtubule plus-end and is thus not transported by accumulating there.

5. LABELED DYNEIN IS INVOLVED IN GENERATING CORTICAL PULLING FORCES.

5.1. TUBE ASSAY IN THE STRAIN DOUBLY LABELED WITH MEMBRANE AND DYNEIN.

We used the previously described "tube assay" (Redemann *et al.*, 2010) to uncover force-generating sites and to see whether labeled DYCI-1 was involved in these events. In embryos treated with *nmy-2(RNAi)* thus having the actin-myosin cortex weakened, we observed colocalization of invagination and DYCI-1::mCherry (see main text, Figure 3D-F). But interestingly, in those without treatment, we also observed 22 ± 13 invaginations (N = 20 embryos), with a frequency occurrence of 0.51 ± 0.07 s^{-1} during anaphase. This compares to 9 ± 7 invaginations and a frequency of 0.23 ± 0.03 s^{-1} in the control strain with only PLCδ1-PH::GFP labeling (N = 11 embryos). The invagination count obtained in the non-treated DYCI-1::mCherry strain is also larger than previously reported for non-treated embryos (Redemann *et al.*, 2010). More importantly, we observed that 42 ± 7% of membrane invaginations are dynein-decorated in these untreated embryos (N = 8 embryos, 84 invaginations). In conclusion, because of the good colocalization of dynein and

invaginations, with or without a weakened actomyosin cortex, we suggest that labeled dynein may be involved in cortical pulling force generation.

Why were half of the invaginations not visibly tagged by DYCI-1::mCherry? It is likely that they contained an amount of DYCI-1::mCherry that fell below our detection limit. The physics of invaginations were studied *in vitro,* and force in the order of tens of pN could be sufficient to pull an invagination (Dernyi *et al.*, 2002; Leduc *et al.*, 2004). The stall force for a dynein is estimated at 6 pN (Howard, 2001). Our detection threshold is estimated to be 26 dyneins (see 2.6 above), much higher than the number of dyneins required to produce a threshold force to pull an invagination. It is therefore probable that some invaginations had dynein counts below this threshold. We concluded that DYCI-1::mCherry correctly reports the dyneins relevant to cortical force generation, and it is therefore appropriate to investigate dynein localizations and dynamics using this strain.

6. DYNAMICS OF DYNEIN AT THE CORTEX AND FORCE GENERATION.

6.1. MEASURING DYNEIN RESIDENCE TIME AT THE CORTEX.

To measure the residence time of DYCI-1::mCherry at the cortex, we imaged the embryo during metaphase at the cortex plane, moving the focus down until the embryo shape appeared diffuse. Next, the focus was moved up less than one micron to recover the embryo shape, and set to this plane for imaging. The detected spots were tracked with u-track software and classified into two populations: direct and diffusive-like (see 2.2-3). In every embryo, we then computed the histogram of track durations for each population, only taking into account tracks longer than 3 frames (600 ms). We estimated the residence time to be the characteristic time $\mu = 1/\lambda$ by fitting the averaged histograms into an exponential distribution (Figure 4D):

$$\frac{1}{\lambda} e^{-\frac{1}{\lambda}t} \tag{S4}$$

where t represents time. Finally, we plotted the distribution of the obtained characteristic times for all embryos and compared the mean per track motion type to establish statistical significance (Figure 4C).

6.2. ANALYSIS OF CORTICAL PULLING FORCE IMBALANCE USING THE TUG-OF-WAR MODEL

As a supplement to the analysis of dynein dynamics at the cortex, we used oscillations to study the mechanism causing the cortical pulling force imbalance. We began by comparing the oscillations of both centrosomes during anaphase. Indeed, because the spindle is weakened in early anaphase (Maton *et al.*, 2015; Mercat *et al.*, 2016), the coupling of the oscillations of both poles is reduced, and thus some differences can be observed between the anterior and posterior sides. In this comparison, we only investigated the amplitude and frequency. We have modeled these oscillations, and proposed that the amplitude positively depends mostly on the so-called negative damping Ξ, while the frequency scales inversely according to the square root of inertia, I (Pecreaux *et al.*, 2006):

$$\begin{aligned} \Xi &= 2N\left(\frac{\overline{f}}{f_c}\overline{p}\left(\left(1-\overline{p}\right)-\frac{f_c}{\overline{f}}\right)\right)f' \\ I &= 2N\left(\frac{\overline{f}}{f_c}\overline{p}\left(1-\overline{p}\right)\right)f'\tau \end{aligned} \tag{S5}$$

N is the number of force generators, and would be different in the cortex halves upon asymmetrical total counts. $\overline{p}$ is the fraction of force generators pulling at a given time; and $\overline{\tau}$ is a time lag. These two parameters only depend on force generator dynamics, and their asymmetry points to

possibilities 1 and 2 discussed in the main text. Finally, $\overline{f}$ is the generator stall force, which corresponds roughly to the force per generator because they act at very low speed, thus close to stall force. This is due to the force-velocity relationship, which states that the pulling force of a generator is inversely proportional to its velocity, with a slope f'. f_c is the detachment rate's sensitivity to force, and the larger that this is, the less the force generator will detach when the pulling force increases. These last three parameters model the intrinsic properties of the force generator (possibility 3 in the main text).

Testing an imbalance of intrinsic force-generator properties (alternative 3)

The model enabled us to predict changes in amplitude and frequency of oscillations when one of the three parameters corresponding to possibility 3 in the model changes (see Supplemental Table S3). The direction indicated corresponds to a higher force on the posterior side, which will ensure spindle displacement (Pecreaux *et al.*, 2006):

Parameter (posterior vs anterior)	Stall force, increased on posterior	Force-velocity slope, increased on posterior	Detachment force sensitivity, increased on posterior
Frequency	Decreased	Decreased	Increased
Amplitude	Increased	Increased	Decreased

Supplemental Table S3: Tug-of-war model predictions for increases in posterior force due to an asymmetry in intrinsic force-generator (dynein) properties (alternative 3).

To challenge this prediction and decide whether the possibility is plausible, we investigated oscillations in untreated embryos (same as Figure 3A), measuring peak-to-peak oscillation amplitudes at 6.0 ± 1.3 μm (mean ± SD) on the posterior, and 3.1 ± 1.1 μm on the anterior (N = 20). The frequencies were 47.3 ± 7.0 mHz and 44.8 ± 6.0 mHz, respectively. We then asked whether the asymmetry could be caused by intrinsic force generator parameter differences (possibility 3). Although the frequency measurements are not significantly different, likely due to the remaining coupling of posterior and anterior centrosomal oscillations by the spindle, the amplitude and frequency are reduced in the anterior versus the posterior sides, while the above prediction suggests that the quantities should vary in opposite directions. Therefore, the observed oscillations are not very compatible with a force imbalance caused by an asymmetry in the intrinsic force generator properties. In support of this, asymmetries in stall forces and force-velocity relationships do not result in asymmetrical active generator counts, in disagreement with previously published results (Grill *et al.*, 2003). Secondly, an asymmetry in force sensitivity would result in generators pulling for a longer time on the posterior side, thus residing longer there, which contradicts our results at the cortex (main text, Figure 5C). Overall, it is unlikely that the force imbalance relies on an asymmetry of intrinsic force generator properties.

Testing an imbalance of the total number of dynein at the cortex.

We next asked whether the force imbalance could be based on the presence of more force generators on the posterior side (total number asymmetry). In this scenario, we expect to have larger oscillations and forces on the posterior side, but also more inertia, thus smaller frequencies. This can be seen by considering that N and f' play similar roles in the equations. In conclusion, since in our experiments the frequencies and amplitudes positively correlate between the posterior and anterior sides, the asymmetry is probably based on dynamics. This conclusion is further supported by the symmetric inflows of dynein at both the anterior and posterior cortices (main text).

Testing an imbalance of dynein dynamics (binding or unbinding, possibilities 1 and 2)

We therefore examined whether force imbalance based on attachment/detachment dynamics (on- and off-rates) could account for the observed oscillation phenotype. The dynein detachment rate at the stall force, also called the off-rate, is modeled by $\overline{k_{off}}$, which is, in turn, part of the calculation of average probability $\overline{p} = k_{on} \Big/ \left(k_{on} + \overline{k_{off}}\right)$ and that of the time lag $\overline{\tau} = 1 \Big/ \left(k_{on} + \overline{k_{off}}\right)$. The higher forces on the posterior side, which contribute to the posterior displacement of the spindle, require a lower detachment rate for that side. Alternatively, if the attachment rate (or the on-rate) is what accounts for the asymmetry, it should be higher on the posterior side to account for the force imbalance. Processivity (the inverse of the off-rate) is likely to control mitotic progression throughout anaphase (Pecreaux *et al.*, 2006). Therefore, an asymmetry in the detachment rate would result in a heterochrony in oscillations, since our model is linearized. In contrast, in addition to a heterochrony, an asymmetry in attachment rates would result in a higher frequency on the posterior side, assuming that processivity controls progression in the same way for both embryo halves. This is consistent with our measurements. In fact, the small difference between frequencies combined with the limitations of the model led us to conclude that both attachment and detachment rate asymmetries could account for force imbalance. Direct measurements of dynein dynamics at the cortex (Figure 5) allowed us to decide in favor of an on-rate asymmetry (main text).

7. REFERENCES

Akhmanova, A., and Steinmetz, M.O. (2015). Control of microtubule organization and dynamics: two ends in the limelight. Nat Rev Mol Cell Biol *16*, 711-726.

Barbosa, D.J., Duro, J., Prevo, B., Cheerambathur, D.K., Carvalho, A.X., and Gassmann, R. (2017). Dynactin binding to tyrosinated microtubules promotes centrosome centration in *C. elegans* by enhancing dynein-mediated organelle transport. PLoS Genet *13*, e1006941.

Bieling, P., Laan, L., Schek, H., Munteanu, E.L., Sandblad, L., Dogterom, M., Brunner, D., and Surrey, T. (2007). Reconstitution of a microtubule plus-end tracking system *in vitro*. Nature *450*, 1100-1105.

Boulin, T., and Bessereau, J.L. (2007). Mos1-mediated insertional mutagenesis in *Caenorhabditis elegans*. Nat Protoc *2*, 1276-1287.

Cockell, M.M., Baumer, K., and Gonczy, P. (2004). lis-1 is required for dynein-dependent cell division processes in *C. elegans* embryos. J Cell Sci *117*, 4571-4582.

Costantino, S., Comeau, J.W., Kolin, D.L., and Wiseman, P.W. (2005). Accuracy and dynamic range of spatial image correlation and cross-correlation spectroscopy. Biophys J *89*, 1251-1260.

Coupe, P., Munz, M., Manjon, J.V., Ruthazer, E.S., and Collins, D.L. (2012). A CANDLE for a deeper *in vivo* insight. Medical Image Analysis *16*, 849-864.

Dernyi, I., Jlicher, F., and Prost, J. (2002). Formation and Interaction of Membrane Tubes. Physical Review Letters *88*, 238101.

Dragestein, K. (2008). Dynamic behavior of GFP–CLIP-170 reveals fast protein turnover on microtubule plus ends, 729-737.

Duellberg, C., Trokter, M., Jha, R., Sen, I., Steinmetz, M.O., and Surrey, T. (2014). Reconstitution of a hierarchical +TIP interaction network controlling microtubule end tracking of dynein. Nat Cell Biol *16*, 804-811.

Grill, S.W., Howard, J., Schaffer, E., Stelzer, E.H., and Hyman, A.A. (2003). The distribution of active force generators controls mitotic spindle position. Science *301*, 518-521.

Howard, J. (2001). Mechanics of motor proteins and the cytoskeleton. Sinauer Associates, Publishers: Sunderland, Mass.

Huet, S., Karatekin, E., Tran, V.S., Fanget, I., Cribier, S., and Henry, J.P. (2006). Analysis of transient behavior in complex trajectories: application to secretory vesicle dynamics. Biophysical Journal *91*, 3542-3559.

Jaqaman, K., Kuwata, H., Touret, N., Collins, R., Trimble, W.S., Danuser, G., and Grinstein, S. (2011). Cytoskeletal control of CD36 diffusion promotes its receptor and signaling function. Cell *146*, 593-606.

Jaqaman, K., Loerke, D., Mettlen, M., Kuwata, H., Grinstein, S., Schmid, S.L., and Danuser, G. (2008). Robust single-particle tracking in live-cell time-lapse sequences. Nat Methods *5*, 695-702.

Kamath, R.S., Fraser, A.G., Dong, Y., Poulin, G., Durbin, R., Gotta, M., Kanapin, A., Le Bot, N., Moreno, S., Sohrmann, M., Welchman, D.P., Zipperlen, P., and Ahringer, J. (2003). Systematic functional analysis of the *Caenorhabditis elegans* genome using RNAi. Nature *421*, 231-237.

Leduc, C., Campas, O., Zeldovich, K.B., Roux, A., Jolimaitre, P., Bourel-Bonnet, L., Goud, B., Joanny, J.F., Bassereau, P., and Prost, J. (2004). Cooperative extraction of membrane nanotubes by molecular motors. Proc Natl Acad Sci U S A *101*, 17096-17101.

Maton, G., Edwards, F., Lacroix, B., Stefanutti, M., Laband, K., Lieury, T., Kim, T., Espeut, J., Canman, J.C., and Dumont, J. (2015). Kinetochore components are required for central spindle assembly. Nat Cell Biol *17*, 697-705.

Mercat, B., Pinson, X., Fouchard, J., Mary, H., Pastezeur, S., Alayan, Z., Gachet, Y., Tournier, S., Bouvrais, H., and Pecreaux, J. (2016). Spindle Micro-Fluctuations of Length Reveal its Dynamics Over Cell Division. Biophysical Society meeting, Los Angeles (CA), USA, *110*, 622a.

Mi, H., Dong, Q., Muruganujan, A., Gaudet, P., Lewis, S., and Thomas, P.D. (2010). PANTHER version 7: improved phylogenetic trees, orthologs and collaboration with the Gene Ontology Consortium. Nucleic acids research *38*, D204-210.

Mi, H., Muruganujan, A., Casagrande, J.T., and Thomas, P.D. (2013). Large-scale gene function analysis with the PANTHER classification system. Nat. Protocols *8*, 1551-1566.

Pecreaux, J., Roper, J.C., Kruse, K., Julicher, F., Hyman, A.A., Grill, S.W., and Howard, J. (2006). Spindle oscillations during asymmetric cell division require a threshold number of active cortical force generators. Curr Biol *16*, 2111-2122.

Redemann, S., Pecreaux, J., Goehring, N.W., Khairy, K., Stelzer, E.H., Hyman, A.A., and Howard, J. (2010). Membrane invaginations reveal cortical sites that pull on mitotic spindles in one-cell *C. elegans* embryos. PLoS One *5*, e12301.

Robert, V., and Bessereau, J.L. (2007). Targeted engineering of the *Caenorhabditis elegans* genome following Mos1-triggered chromosomal breaks. Embo J *26*, 170-183.

Sage, D., Neumann, F.R., Hediger, F., Gasser, S.M., and Unser, M. (2005). Automatic tracking of individual fluorescence particles: application to the study of chromosome dynamics. IEEE Transactions on Image Processing *14*, 1372-1383.

Sarov, M., Murray, J.I., Schanze, K., Pozniakovski, A., Niu, W., Angermann, K., Hasse, S., Rupprecht, M., Vinis, E., Tinney, M., Preston, E., Zinke, A., Enst, S., Teichgraber, T., Janette, J., Reis, K., Janosch, S., Schloissnig, S., Ejsmont, R.K., Slightam, C., Xu, X., Kim, S.K., Reinke, V., Stewart, A.F., Snyder, M., Waterston, R.H., and Hyman, A.A. (2012). A genome-scale resource for in vivo tag-based protein function exploration in *C. elegans*. Cell *150*, 855-866.

Sarov, M., Schneider, S., Pozniakovski, A., Roguev, A., Ernst, S., Zhang, Y., Hyman, A.A., and Stewart, A.F. (2006). A recombineering pipeline for functional genomics applied to *Caenorhabditis elegans*. Nat Methods *3*, 839-844.

Schmidt, R., Fielmich, L.E., Grigoriev, I., Katrukha, E.A., Akhmanova, A., and van den Heuvel, S. (2017). Two populations of cytoplasmic dynein contribute to spindle positioning in *C. elegans* embryos. J Cell Biol *216*, 2777-2793.

Shivaraju, M., Unruh, J.R., Slaughter, B.D., Mattingly, M., Berman, J., and Gerton, J.L. (2012). Cell-cycle-coupled structural oscillation of centromeric nucleosomes in yeast. Cell *150*, 304-316.

Skop, A.R., and White, J.G. (1998). The dynactin complex is required for cleavage plane specification in early *Caenorhabditis elegans* embryos. Curr Biol *8*, 1110-1116.

Sonnichsen, B., Koski, L.B., Walsh, A., Marschall, P., Neumann, B., Brehm, M., Alleaume, A.M., Artelt, J., Bettencourt, P., Cassin, E., Hewitson, M., Holz, C., Khan, M., Lazik, S., Martin, C., Nitzsche, B., Ruer, M., Stamford, J., Winzi, M., Heinkel, R., Roder, M., Finell, J., Hantsch, H., Jones, S.J., Jones, M., Piano, F., Gunsalus, K.C., Oegema, K., Gonczy, P., Coulson, A., Hyman, A.A., and Echeverri, C.J. (2005). Full-genome RNAi profiling of early embryogenesis in *Caenorhabditis elegans*. Nature *434*, 462-469.

Srayko, M., Kaya, A., Stamford, J., and Hyman, A.A. (2005). Identification and characterization of factors required for microtubule growth and nucleation in the early *C. elegans* embryo. Dev Cell *9*, 223-236.

Widengren, J., Rigler, R., and Mets, U. (1994). Triplet-state monitoring by fluorescence correlation spectroscopy. Journal of fluorescence *4*, 255-258.